



저작자표시-비영리-변경금지 2.0 대한민국

이용자는 아래의 조건을 따르는 경우에 한하여 자유롭게

- 이 저작물을 복제, 배포, 전송, 전시, 공연 및 방송할 수 있습니다.

다음과 같은 조건을 따라야 합니다:



저작자표시. 귀하는 원저작자를 표시하여야 합니다.



비영리. 귀하는 이 저작물을 영리 목적으로 이용할 수 없습니다.



변경금지. 귀하는 이 저작물을 개작, 변형 또는 가공할 수 없습니다.

- 귀하는, 이 저작물의 재이용이나 배포의 경우, 이 저작물에 적용된 이용허락조건을 명확하게 나타내어야 합니다.
- 저작권자로부터 별도의 허가를 받으면 이러한 조건들은 적용되지 않습니다.

저작권법에 따른 이용자의 권리는 위의 내용에 의하여 영향을 받지 않습니다.

이것은 [이용허락규약\(Legal Code\)](#)을 이해하기 쉽게 요약한 것입니다.

[Disclaimer](#)

공학석사학위논문

벽 부착 캐비테이션 기포의 붕괴에 관한
수치해석

**Numerical analysis on the collapse of
wall-attached cavitation bubble**

2023 년 2 월

서울대학교 대학원

기계공학부

오 혜 정

벽 부착 캐비테이션 기포의 붕괴에 관한 수치해석

Numerical analysis on the collapse of wall-attached cavitation bubble

지도교수 최 해 천

이 논문을 공학석사 학위논문으로 제출함

2022 년 10 월

서울대학교 대학원

기계공학부

오 혜 정

오혜정의 공학석사 학위논문을 인준함

2022 년 12 월

위 원 장	<u>송 성 진</u>
부위원장	<u>최 해 천</u>
위 원	<u>김 호 영</u>

Numerical analysis on the collapse of wall-attached cavitation bubble

Oh Hyejeong

Department of Mechanical Engineering

Seoul National University

Abstract

In the present study, we numerically investigate the spherical and ellipsoidal bubbles in the situation where the bubble is attached to walls. The simulations are conducted with an incompressible two-phase flow solver. We adopt a geometrical volume of fluid method to accurately track bubble interfaces in rapid changes during cavitation and calculate the liquid and vapor phase using a transport equation model with cavitation model. We validate this model by solving Rayleigh bubble collapse problem and the results are consistent with the analytical solution. Subsequently, the wall-attached cavitation bubble is simulated for a fixed wall distance condition. For the spherical bubble, the numerical results are in well agreement with the experimental results, and the bubble collapses into a torus shape as the jet impact on the wall spreads radially outward from the center of the wall. For the ellipsoidal bubble, parametric study is conducted about the initial aspect ratio. In the collapse of the ellipsoidal bubble, two different jets occur, and the initial aspect ratio determines the relative behavior between them. The faster one dominates the collapse pattern, and the ellipsoidal bubble collapses into

two pieces, forming a lung-like shape. The jet impact on the wall spreads from the center of the wall in the direction of the major axis of the bubble. On the other hand, in the case of ellipsoidal bubbles with a nearly spherical aspect ratio, the magnitude of the dominant jet is relatively small and its position changes with time, resulting in an asymmetrical torus shape. From these results, we conclude that collapse pattern of the bubble significantly depends on the position and the relative magnitude of the dominant jet which are determined by the aspect ratio, and present the detailed flow characteristics numerically.

keywords: numerical simulation, two-phase flow, cavitation, bubble collapse

student number: 2021-29710

Contents

Abstract	i
Contents	iii
List of Tables	v
List of Figures	vi
1 Introduction	1
2 Methodology	4
2.1 Governing equations	4
2.2 VOF-PLIC method	6
2.3 Cavitation model	8
3 Rayleigh bubble collapse	10
3.1 Setup	11
3.2 Results and discussion	12
4 Wall-attached bubble collapse	15
4.1 Setup	15

4.2	Results and discussion	16
4.2.1	Spherical bubble	16
4.2.2	Ellipsoidal bubble	20
4.2.3	Effect of aspect ratio	22
5	Conclusion	26

List of Tables

2.1	Fluid properties	9
2.2	User parameters for phase change rate	9

List of Figures

2.1	A bubble interface (white solid line) and distribution of liquid volume fraction near the interface	7
2.2	Actual and PLIC reconstructed interfaces (blue solid line) in 2D plane and fluxes in x direction during the time step.	8
3.1	Computational domain, boundary conditions, and initial conditions . .	11
3.2	Evolution of the bubble radius	12
3.3	Evolution of the bubble interface	13
3.4	Evolution of liquid pressure distribution in radial direction	14
4.1	Computational domain, boundary conditions, and initial conditions . .	16
4.2	Collapse pattern of a wall-attached spherical bubble (1st row - photograph: experimental results, white dot line: numerical results in 2D; 2nd row - numerical results in 3D)	17
4.3	Interfaces of spherical bubble (black solid line) and position of the maximum jet (red arrow) in yz cross-section	17
4.4	Maximum jet speed for spherical bubbles	18
4.5	Jet impact on the wall for spherical bubbles	18
4.6	Collapse mechanism of wall-attached bubble	19

4.7	Interfaces of ellipsoidal bubble (black solid line) and position of the maximum jet (red arrow) and y-axis jet (black arrow) in yz and xy cross-section	20
4.8	Maximum and y-axis jet speeds for ellipsoidal bubble	21
4.9	Jet impact on the wall for ellipsoidal bubbles	22
4.10	Collapse pattern of wall-mounted bubbles for all AR cases	23
4.11	Magnitude difference between maximum jet and y-axis jet for all AR cases	24
4.12	Interfaces of ellipsoidal bubble (black solid line) and position of the maximum jet (red arrow) and y-axis jet (black arrow) in yz cross-section (AR=1.1)	25
4.13	Interfaces of ellipsoidal bubble (black solid line) and position of the maximum jet (red arrow) and y-axis jet (black arrow) in yz cross-section (AR=1.2)	25

Chapter 1

Introduction

Cavitation is a phenomenon that vapor bubbles occurs when the local pressure in a liquid flow falls below the vapor pressure. The collapse of the vapor bubble can cause erosion on the walls of technical devices. During the collapse, a dominant jet develops, and this pattern depends on the geometric conditions between the bubble and walls (Lauterborn and Bolle, 1975; Philipp and Lauterborn, 1998; Zhang et al., 2017). Recently, cavitation bubbles are intentionally generated by laser technologies to utilize these characteristics for biomedical or microfluidic operations (Le Gac et al., 2007; Požar et al., 2021).

The analysis of bubble collapse is a challenging topic because it is difficult to measure physical properties experimentally. The difficulties are caused by the extremely small temporal and spatial scale of the bubble collapse. From these reasons, many numerical simulations have conducted on the cavitation bubble collapse to provide detail flow configurations which are difficult to obtain by experiments. Trummel et al. (2021) studied the generic configurations of cavitation bubble with different stand-off distances. Nguyen et al. (2022) analyzed the water jet and impact pressure for the bub-

ble collapse near an oblique wall and free surface with comparing to the experiments of Zhang et al. (2017). Rodriguez et al. (2022) examined the dependence of the dynamics on the initial bubble position between two parallel and rigid walls.

Previous studies generally have assumed the initially spherical bubble and examined the effect of the bubble-wall structure. However, the numerical study on the effect of the bubble shape have not yet been fully investigated, although the cavitation bubble is most likely to extend horizontally or vertically in the real applications and may be elliptical for laser-induced bubbles (Lim et al., 2010; Sagar and el Moctar, 2020). Few studies have reported the effect of the bubble shape on the collapse. Lauer et al. (2012) analyzed wall pressures for the horizontally elongated ellipsoidal bubble attached to the wall and Aganin et al. (2016) presented the interface velocity for the ellipsoidal bubble which places on the wall. In these studies, they have only considered simple situations that the re-entrant jet, also called a dominant jet, flows parallel to the axis. However, we can expect different bubble collapse patterns from the past results because the orientation of the dominant jet varies depending on the geometric condition between the bubble and the wall.

Therefore, the objective of this study is to investigate the effect of non-spherical shape of the wall-attached bubble on collapse patterns under the condition in which the dominant jet is not parallel to the axis. For a numerical model, we employ a geometric volume of fluid (VOF) method (Nguyen and Park, 2016, 2017) and transport equation model (TEM) (Schnerr and Sauer, 2001) based on an incompressible and isothermal two-phase flow solver. The geometric VOF method is used to calculate two-phase interfaces by considering the geometrical reconstruction of the interface and its flux based on a liquid volume fraction at every time step. This ensures a sharp interface and mass conservation without any artificial terms and mass corrections. In the

TEM, a transport equation is solved with the source term considering a phase change. By considering the phase change at interfaces, it makes possible to mimic the cavitation process in the incompressible and isothermal two-phase flow solver. All simulation models are based on the `interPhaseChangeFoam` in the open source C++ package OpenFOAM (Weller et al., 1998). To validate the numerical model, Rayleigh bubble collapse test is conducted (Franc and Michel, 2006). To study the effect of non-spherical shape on the bubble collapse, parametric study is performed about the aspect ratio when the bubble is attached to the wall. From the results, we present the collapse pattern by analyzing the position and the relative magnitude of dominant jet and discuss the significance of the effect of the bubble shape on the bubble collapse.

Chapter 2

Methodology

2.1 Governing equations

In the present simulation, continuity and momentum equations are solved for the mixture of liquid and vapor under the assumption that each liquid and vapor phases are incompressible and isothermal. In addition, a transport equation is solved to track the liquid-vapor interfaces. This ensures the mass conservation without any treatments (Nguyen and Park, 2016). These equations are solved based on the liquid-vapor mixture. Each liquid and vapor phase is considered incompressible, but the mixture density depends on the change in the liquid volume fraction by cavitation in this study. Thus, the continuity equation is given by

$$\nabla \cdot \mathbf{u} = \left(\frac{1}{\rho_l} - \frac{1}{\rho_v}\right)\dot{m}, \quad (2.1)$$

where ρ_l is the liquid density and ρ_v is the vapor density, and \dot{m} is phase change rate.

The momentum equation is given by

$$\frac{\partial \rho \mathbf{u}}{\partial t} + \nabla \cdot (\rho \mathbf{u} \mathbf{u}) = -\nabla p + \nabla \cdot [\mu(\nabla \mathbf{u} + \nabla \mathbf{u}^T)], \quad (2.2)$$

where \mathbf{u} is the velocity vector, p is pressure, ρ is the mixture density, and μ is the mixture viscosity. Here, we ignore the surface tension due to the large pressure difference between the vapor and liquid. It can be derived from the following collapse rate equation,

$$\frac{dR}{dt} = -\sqrt{\frac{2}{3} \frac{\Delta p}{\rho} \left(\frac{R_0^3}{R^3} - 1 \right) + \frac{2\sigma}{\rho R_0} \frac{R_0^3}{R^3} \left(1 - \frac{R^2}{R_0^2} \right)}, \quad (2.3)$$

where the pressure difference Δp is about $10^5 Pa$, the initial bubble radius R_0 is $0.001m$, and the surface tension σ is $0.072N/m$ in the this study. Based on this condition, the effect of surface tension is neglected because the coefficient of the first term is much larger than that of the second term (Franc and Michel, 2006).

From the above two governing equations, the velocity and pressure field is solved, and the following transport equation is solved.

$$\frac{\partial \alpha}{\partial t} + \nabla \cdot (\mathbf{u}\alpha) = \frac{\dot{m}}{\rho_l}, \quad (2.4)$$

where the liquid volume fraction α means the amount of liquid present in a computational cell relatively, and the phase change rate \dot{m} is included on the right-hand side of the equation. The liquid volume fraction will be discussed in relation to the volume of fluid method in section 2.2. To close the equations (2.1), (2.4), the phase change rate \dot{m} should be determined, and it will be presented in section 2.3.

2.2 VOF-PLIC method

In the volume of fluid (VOF) method, as shown in section 2.1, the liquid volume fraction α defines the phase state and mixture properties of each computational cell and the transport equation (Eq. (2.4)) is solved to calculate the liquid volume fraction α in each time step. The phase state is defined by the liquid volume fraction α as follows,

$$\alpha(x, t) = \begin{cases} 1 & \text{liquid} \\ > 0, < 1 & \text{interface} \\ 0 & \text{vapor.} \end{cases} \quad (2.5)$$

Based on the liquid volume fraction, the mixture properties, e.g. density and dynamic viscosity, are expressed as

$$\rho = \rho_v \alpha + \rho_l (1 - \alpha), \quad (2.6)$$

$$\mu = \mu_v \alpha + \mu_l (1 - \alpha). \quad (2.7)$$

By using the following distribution function about the liquid volume fraction, bubble interfaces can be expressed by finite values in each cell.

$$\alpha(r) = 1 - \frac{1}{2} \left[1 - \tanh \left(\frac{r - R_0}{C \Delta x} \right) \right] \quad (2.8)$$

Eq. 2.8 presents the hyperbolic tangent function, and the constant C determines the width of the interface. In the Eq. 2.8, R_0 is the initial bubble radius, r is the radial distance from the bubble center O , and Δx is the computational cell size. Fig. 2.1 shows the distribution of the liquid volume fraction according to the function. Several cells within the interface region have liquid volume fraction greater than 0 and less than 1, and the contour line corresponding to the liquid volume fraction of 0.5 indicates a bubble interface.

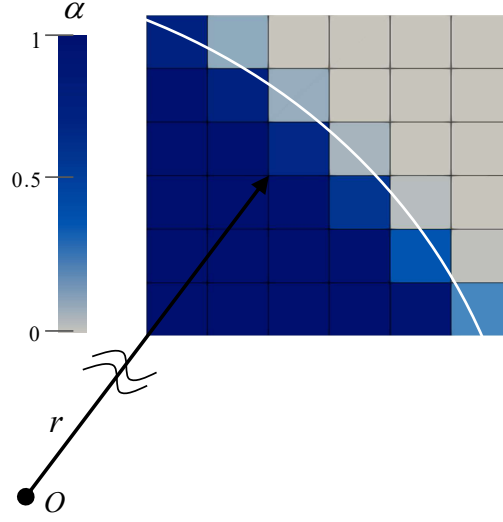


Figure 2.1: A bubble interface (white solid line) and distribution of liquid volume fraction near the interface

To track the interface accurately, a piecewise linear interface calculation (PLIC) method is employed. PLIC method geometrically reconstructs the liquid-vapor interface based on the distribution of the liquid volume fraction. Fig. 2.2 shows the actual and PLIC reconstructed liquid-vapor interfaces and the fluxes in x direction during the time step Δt . In this method, a planar surface function $y = F(x)$, the reconstructed interface, is defined based on liquid volume fraction information of neighboring cells of the cell of interest. We use Youngs method to calculate this function in this study (Youngs, 1982). Based on this function, the flux of liquid volume fraction during the time step, $flux_i$, is calculated by the following equation.

$$flux_{i+1} = \int_{\Delta x - u\Delta t}^{\Delta x} F(x) dx \quad (2.9)$$

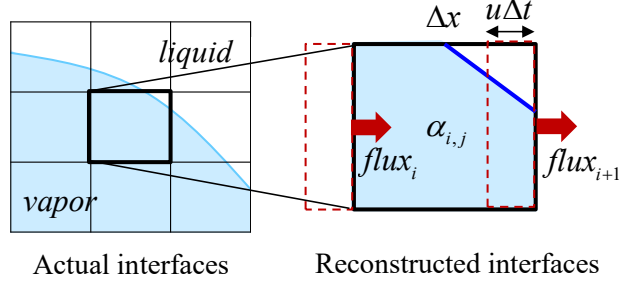


Figure 2.2: Actual and PLIC reconstructed interfaces (blue solid line) in 2D plane and fluxes in x direction during the time step.

2.3 Cavitation model

Cavitation model defines the phase change rates which are correlated to the single bubble dynamics. In the present study, the Schnerr-Sauer model (Schnerr and Sauer, 2001) is adopted. The Schnerr-Sauer model assumes that the vapor consist of spherical bubbles, and therefore the volume of the vapor depends on the number and radius of these bubbles. The behavior, e.g. growth rate, of each bubble is explained by the Rayleigh-Plesset equation. From this equation, both the condensation \dot{m}_c and vaporization \dot{m}_v rates are derived based on the fluid properties. The expressions are represented as follows:

$$\begin{aligned} \dot{m} &= \dot{m}_c + \dot{m}_v, \\ \dot{m}_c &= C_c \alpha (1 - \alpha) \frac{3\rho_l \rho_v}{\rho R_B} \sqrt{\frac{2}{3\rho_l |p - p_v|}} \max(p - p_v, 0), \\ \dot{m}_v &= C_v \alpha (1 + \alpha_N - \alpha) \frac{3\rho_l \rho_v}{\rho R_B} \sqrt{\frac{2}{3\rho_l |p - p_v|}} \min(p - p_v, 0), \end{aligned} \quad (2.10)$$

where p_v is a vapor pressure at which the phase change is assumed to happen and the user defined parameters C_c , C_v controls the rate of the phase changes. α_N and R_B

are the volume fraction of bubble nuclei in the liquid and generic radius, respectively.

These can be obtained from the following equations,

$$\alpha_N = \frac{\frac{\pi n_0 d_N u c^3}{6}}{1 + \frac{\pi n_0 d_N^3}{6}} \quad (2.11)$$

$$R_B = \sqrt[3]{\frac{3}{4\pi n_0} \frac{1 + \alpha_N - \alpha}{\alpha}}. \quad (2.12)$$

where n_0 and d_N are user defined parameters. They correspond to the number of nuclei per cubic meter and the nucleation site diameter, respectively. In this study, fluid properties and user parameters are set as shown in Table 2.1 and Table 2.2.

Table 2.1: Fluid properties

$\rho_l[kgm^{-3}]$	1000
$\rho_v[kgm^{-3}]$	0.0231
$\mu_l[m^2/s]$	9.793*10-7
$\mu_v[m^2/s]$	4.273*10-4

Table 2.2: User parameters for phase change rate

C_c	1000
C_v	1000
n_0	10^8
d_N	10^{-4}

Chapter 3

Rayleigh bubble collapse

The Rayleigh bubble collapse test is conducted as a validation for the present numerical model. In this test, the bubble is supposed to be in equilibrium and immersed in an infinite incompressible fluid at the first phase. From the instant $t = 0$, the high pressure p_∞ applied to the liquid drives the collapse of the bubble at a characteristic time τ called the Rayleigh time.

The analytic solution is derived from the Rayleigh-Plesset equation for this problem (Franc and Michel, 2006). The bubble collapse rate and the liquid pressure evolution are given by

$$\frac{dR}{dt} = -\sqrt{\frac{2}{3} \frac{\Delta p}{\rho} \left(\frac{R_0^3}{R^3} - 1 \right)}, \quad (3.1)$$

$$p^* = \frac{p(r) - p_\infty}{p_\infty - p_v} = \frac{R}{3r} \left[\frac{R_0^3}{R^3} - 4 \right] - \frac{R^4}{3r^4} \left[\frac{R_0^3}{R^3} - 1 \right], \quad (3.2)$$

respectively. In the above equations, r is the radial distance from the center of the bubble, R_0 is the initial bubble radius, and the Δp is the difference between the liquid and vapor pressures.

3.1 Setup

We initialize the vapor bubble with radius $R_0 = 1mm$ and pressure $p_v = 2300Pa$. The initial liquid pressure near the bubble has the distribution derived from the equation (3.2), i.e. p^* for $R = R_0$. The pressure converges to the pressure $p_\infty = 10^5 Pa$ at the far field boundary. The computational domain has the size $L_x = L_y = L_z = 100R_0$. The cells per bubble radius (CPBR) is set to be 100. A fixed condition is used for pressure and a Neumann condition is used for liquid volume fraction and velocity at the far field boundary.

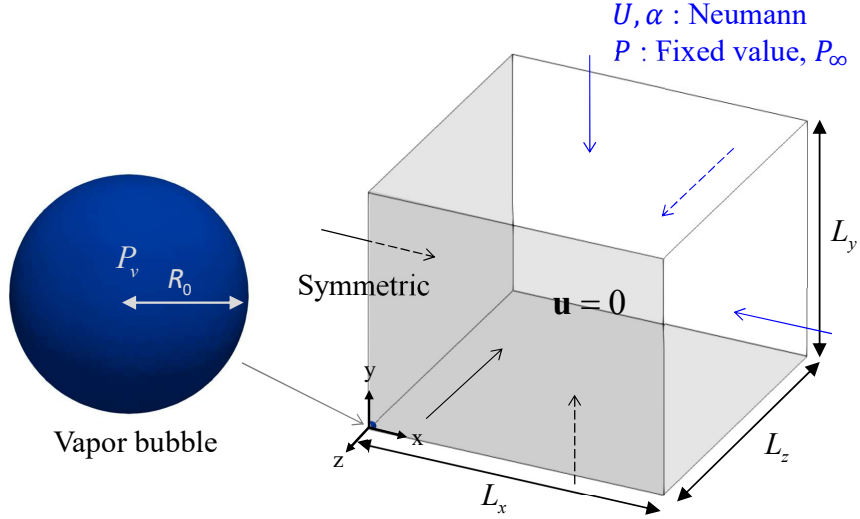


Figure 3.1: Computational domain, boundary conditions, and initial conditions

3.2 Results and discussion

The numerical result is compared with the analytical solution about the evolution of bubble radius and liquid pressure distribution.

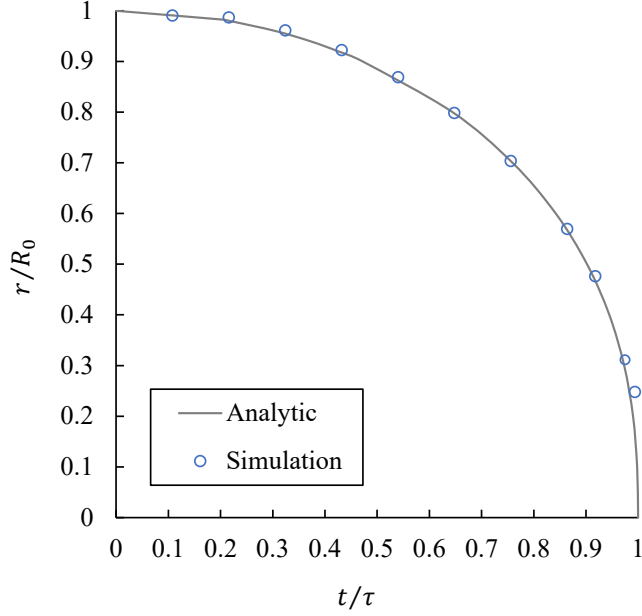


Figure 3.2: Evolution of the bubble radius

The evolution of bubble radius is shown in Figure 3.2. In this figure, the bubble radius is nondimensionalized by the initial radius R_0 and the time is nondimensionalized by Rayleigh collapse time τ . Here, the bubble radius corresponds to the 0.5 value of the liquid volume fraction. The rate of change in the radius increases over time and becomes infinite at the end of the collapse. Also, the Figure 3.3. shows the bubble interfaces at three different normalized times t/τ of 0.6482, 0.8642 and 0.9722 which are corresponding to non-dimensional radius r/R_0 of 0.8, 0.57 and 0.3, respectively. From the Fig. (2) and Fig. (3), it is shown that the numerical results are in good agreement with the analytic solution and the bubble interfaces maintain the circular shape

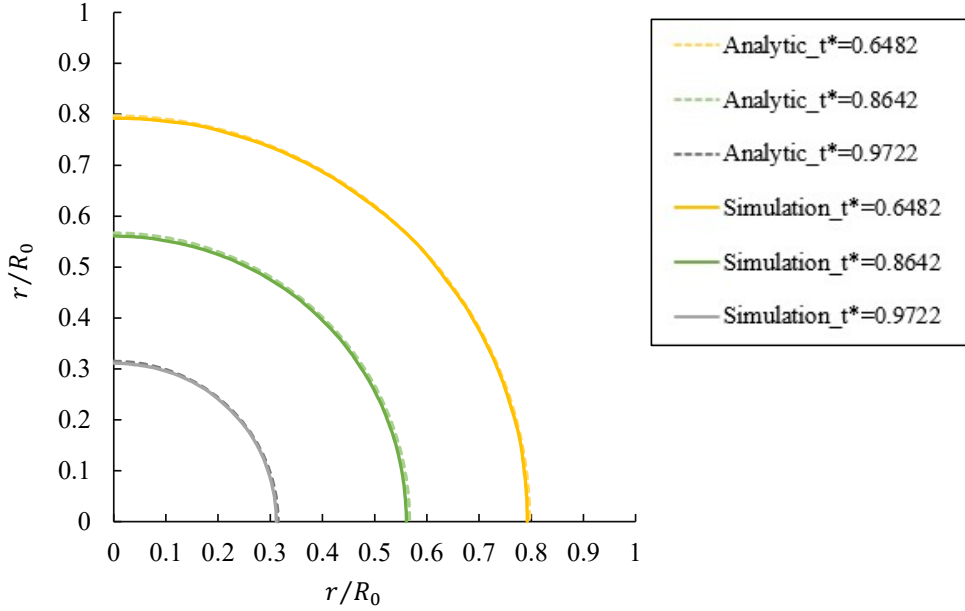


Figure 3.3: Evolution of the bubble interface

without wiggles during collapse. In Figure 3.4., the evolution of liquid pressure distribution in the radial direction is plotted. In this plot, five different normalized times t/τ of 0.6482, 0.7562, 0.8642, 0.9182 and 0.9722 are chosen which are corresponding to non-dimensional radius r/R_0 of 0.8, 0.7, 0.57, 0.47 and 0.3, respectively. The maximum liquid pressure occurs the right outside of bubble interface and the pressure converges to infinite liquid pressure p_∞ as r approaches to the far field boundary. This pressure wave is mainly caused by the effect of inertial forces. The maximum pressure value increases significantly as the bubble collapses while the vapor pressure remains constant. The numerical results follow the analytic solution of the pressure wave distribution

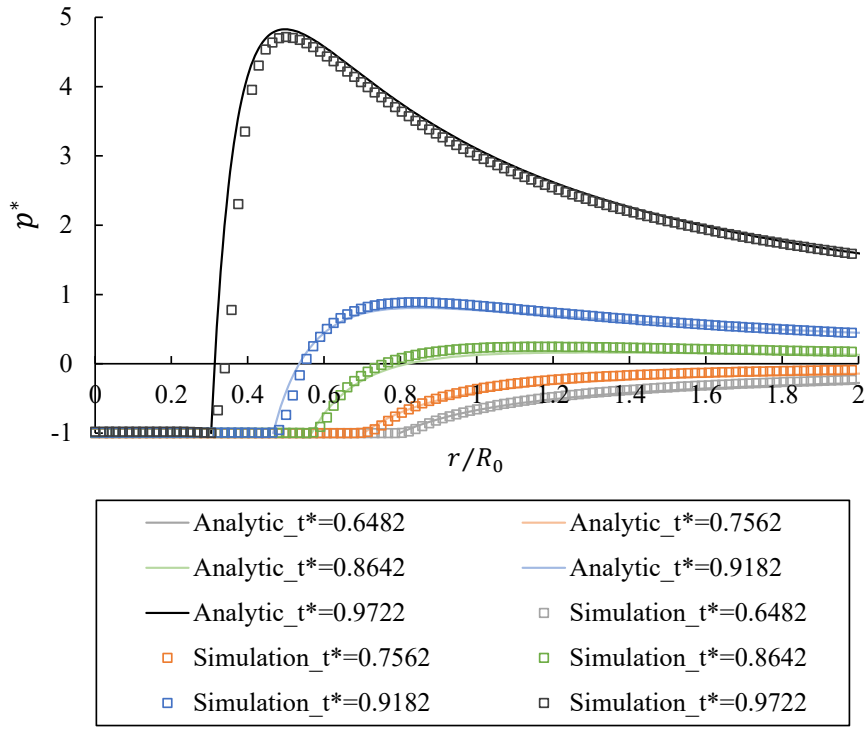


Figure 3.4: Evolution of liquid pressure distribution in radial direction

Chapter 4

Wall-attached bubble collapse

In this section, we investigate the collapse of a wall-attached bubble. In the wall-attached bubble collapse, unlike bubble collapse in the free field, the delay effect of the wall can be observed by the interaction with the wall. In this study, the numerical results of the spherical bubble will first be compared with the corresponding experimental results (Philipp and Lauterborn, 1998). Next, we present the numerical results of ellipsoidal bubbles, and discuss the effect of aspect ratio on the collapse of wall-attached bubbles.

4.1 Setup

We initialize the bubble with radius $R_0 = 1.5mm$ and pressure $p_v = 1000Pa$. The initial liquid pressure near the bubble has the distribution derived from the equation (3.2), i.e. p^* for $R = R_0$. The pressure converges to the pressure $p_\infty = 10^5 Pa$ at the far field boundary. The computational domain has the size $L_x = L_z = 10R_0, L_y = 6R_0$. The cells per bubble radius (CPBR) is set to be 100. The relative wall distance

D/R_0 is 0.3. No slip condition is applied for the bottom boundary and Neumann condition is used for all far field boundaries. The simulated cases of ellipsoidal bubble correspond to the aspect ratios (AR) of 1.1, 1.2, 1.4, 1.7, and 2.0.

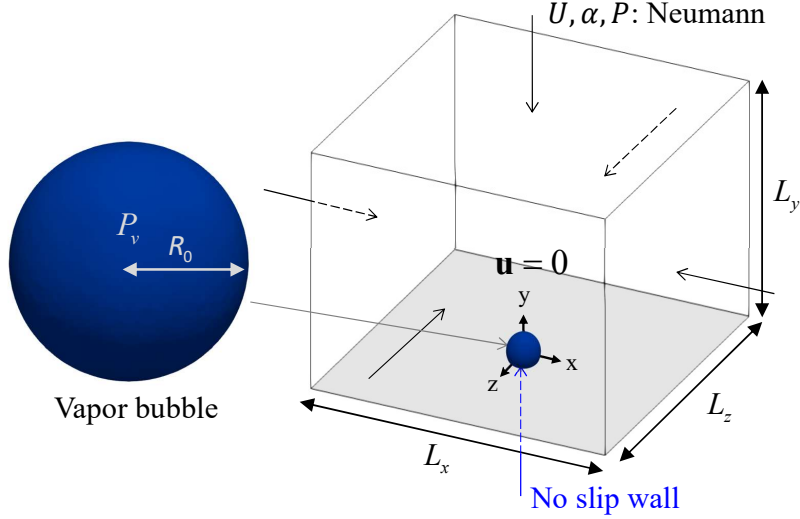


Figure 4.1: Computational domain, boundary conditions, and initial conditions

4.2 Results and discussion

4.2.1 Spherical bubble

This section presents the spherical bubble with $AR=1.0$. Fig. 4.2 shows the collapse pattern of a wall-attached spherical bubble compared with the experimental results. Fig. 4.3 shows the position of the maximum jet and the interface of the bubble in yz cross-section, and Fig. 4.4 plots the maximum jet speed over time. In the velocity plot, the time is nondimensionalized by the collapse time τ , which is the time when the bubble completely collapses, and the velocity is nondimensionalized by the magnitude of the maximum jet tip velocity V_{max}^* which is defined by the velocity at the moment

when the jet hit the lower wall of the bubble.

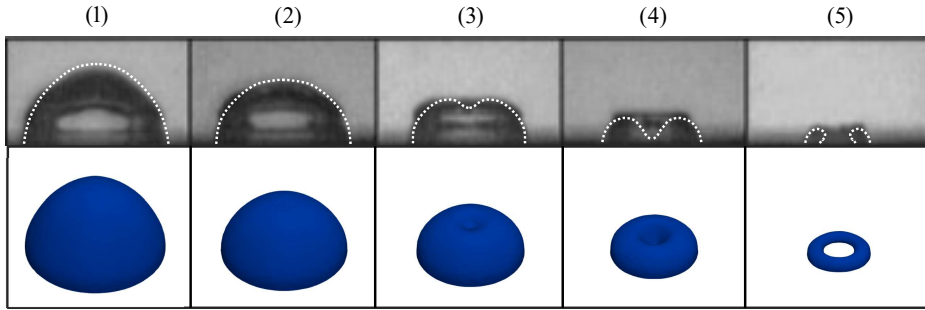


Figure 4.2: Collapse pattern of a wall-attached spherical bubble (1st row - photograph: experimental results, white dot line: numerical results in 2D; 2nd row - numerical results in 3D)

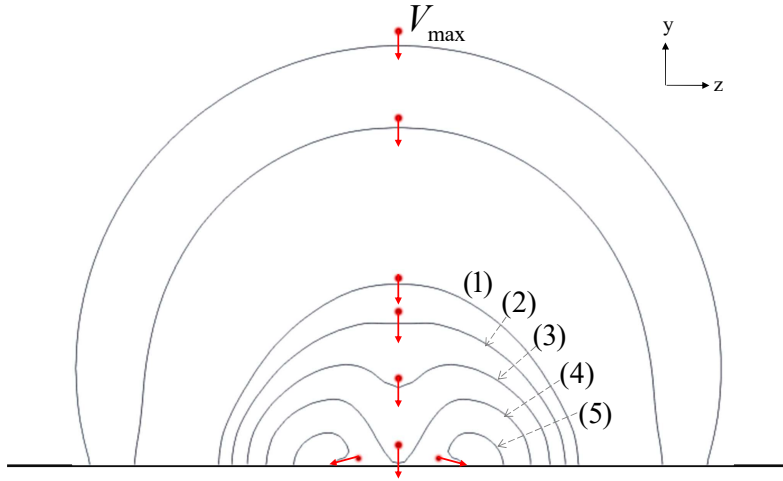


Figure 4.3: Interfaces of spherical bubble (black solid line) and position of the maximum jet (red arrow) in yz cross-section

In general, the numerical simulations are in good agreement with the experimental results. The collapse pattern follows the following sequences. The bubbles initially

form a dome shape, and the upper wall of the bubbles is sequentially flattened and curved toward the wall. Next, the jet from the top hits the wall with reaching the value of the maximum jet tip velocity and then penetrates the bubble. After penetrating, the jet develops radially outwards along the wall and becomes a ring vortex while turning the bubble into a torus shape. In the final stage, the jet velocity reaches the maximum value while making the torus completely collapses from the inner side. From this collapse pattern, the impact on the wall spreads radially outward from the center of the wall as shown in Fig 4.5.

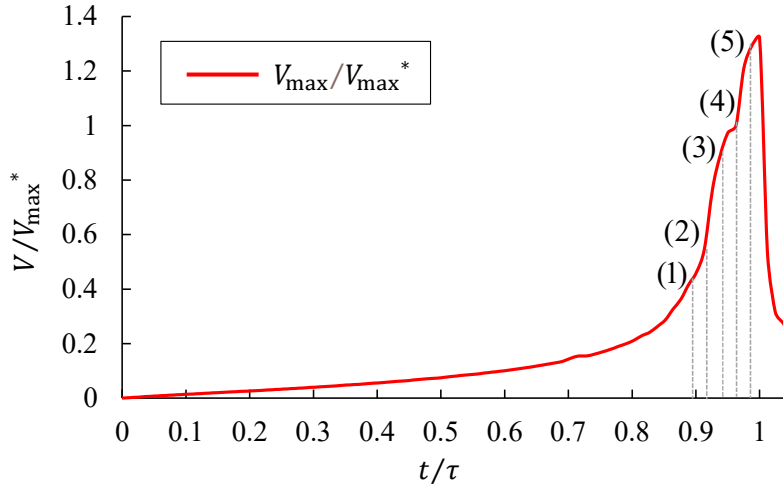


Figure 4.4: Maximum jet speed for spherical bubbles

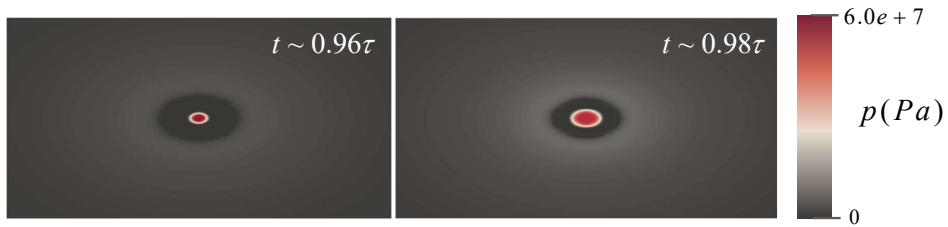


Figure 4.5: Jet impact on the wall for spherical bubbles

From the results, collapse mechanism of wall-attached bubbles can be summarized as shown in Fig. 4.6. The jet basically flows in a radial direction of the bubble. The side of the bubble close to the wall collapses more slowly than the rest due to the effect of the wall, and the top of the bubble collapses much faster than the rest because it has a maximum extension from the wall. Here, this maximum jet from the top, called a dominant jet, dominates the collapse of the bubble.

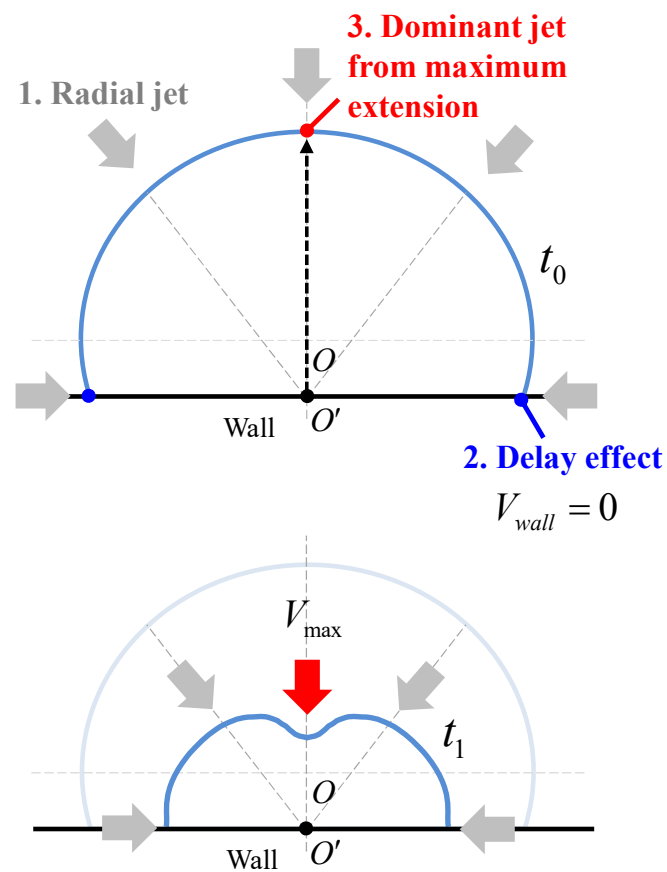


Figure 4.6: Collapse mechanism of wall-attached bubble

4.2.2 Ellipsoidal bubble

This section presents the ellipsoidal bubble with $AR=2.0$ to clearly figure out the difference from the spherical case in collapse patterns. Fig. 4.7 shows the position of the maximum jet V_{max} , the y-axis jet V_{top} and the interface of the bubble in both yz and xy cross-section. Fig. 4.8 shows the maximum jet speed and the y-axis parallel jet over time. The time and velocity are nondimensionalized by the collapse time τ and the maximum jet tip velocity V_{max}^* of the spherical case.

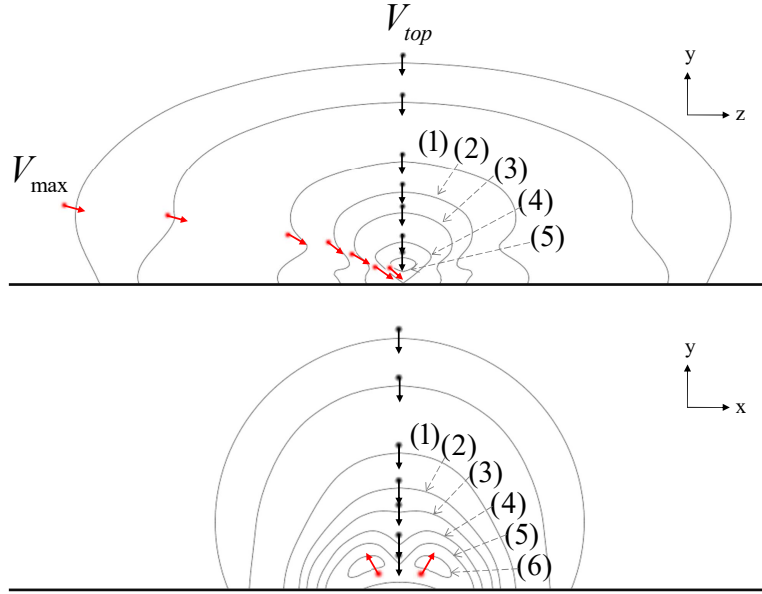


Figure 4.7: Interfaces of ellipsoidal bubble (black solid line) and position of the maximum jet (red arrow) and y-axis jet (black arrow) in yz and xy cross-section

In the case of the ellipsoidal bubble, two different jets should be considered due to the asymmetric shape. One is the jet from the top of the bubble, and the other is the jet from the maximum extension point of the bubble. The maximum extension is the point at which the z-axis passing through the center of the bubble meets the bubble

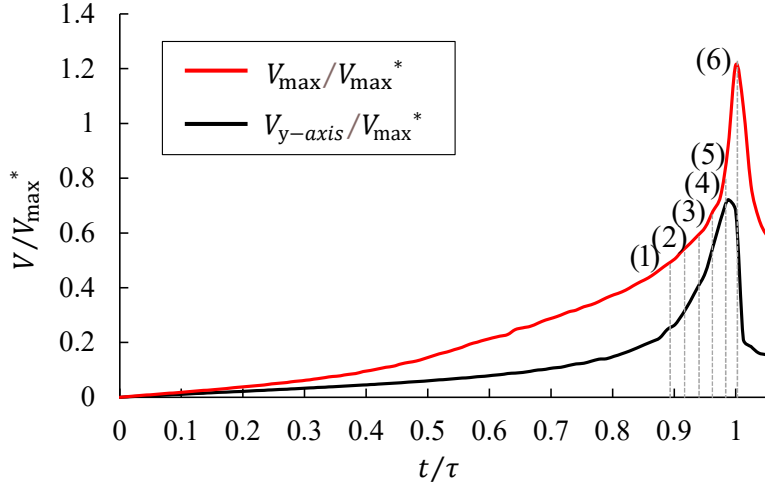


Figure 4.8: Maximum and y-axis jet speeds for ellipsoidal bubble

interface. From this point, the dominant jet develops in the radial direction.

In the early stage, the two jets have the similar magnitude of velocity, and the bubble forms a dome-shape due to the delay effect of the wall with the grooved sides by the dominant jet. As the dominant jet velocity grows much higher than the y-axis parallel jet, the z-axis side of the bubble becomes very curved in the radial direction and the lower side of bubble is penetrated first. At the same time, as shown in the xy cross-section, the jet from the top of the bubble makes the upper wall of bubble flat and then curved because the top of the bubble is a relatively extended point in the xy cross-section. In this situation, the bubble forms a lung-shape where the thin bridge connects the two small bubbles. As the jet develops, the bubble separates into the two pieces, and the maximum jet tip velocity occurs right before the separation. After the separation, the jet develops radially outwards along the wall and makes the bubble completely collapses while reaching the maximum velocity. From this collapse pattern, the jet impacts the wall in an asymmetric way, and the impact spreads from

the center of the wall in the direction of the major axis of the bubble as shown in Fig. 4.9.

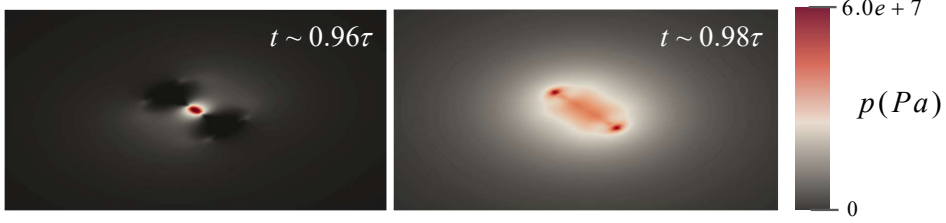


Figure 4.9: Jet impact on the wall for ellipsoidal bubbles

4.2.3 Effect of aspect ratio

As presented in the section 4.2.2, the ellipsoidal bubble collapses in a significantly different way due to the two different jets. In this case, the bubble shape has the high aspect ratio, and it makes the dominant jet from the z-axis parallel maximum extension point highly dominates the bubble collapse. From this result, we could expect that the aspect ratio differs the difference of the magnitude of the two jets and the collapse patterns consequently. Hence, we simulated the cases of ellipsoidal bubble correspond to AR=1.1, 1.2, 1.4, 1.7, and 2.0 to investigate the effect of the aspect ratio.

Fig. 4.10 shows the collapse pattern of wall-attached bubbles for all AR cases. The ellipsoidal bubble with small AR tends to collapse into torus shape in the similar way of the spherical bubble case, and the ellipsoidal bubble with large AR tends to collapse into two pieces. This tendency can be explained by the variation of the position and magnitude of the maximum jet and y-axis jet.

Fig. 4.11 plots the magnitude difference between the maximum jet V_{max} and the y-axis jet V_{top} for all AR cases over time. The difference between the two jets gradually increases with the development of the maximum jet, and decreases because the phase

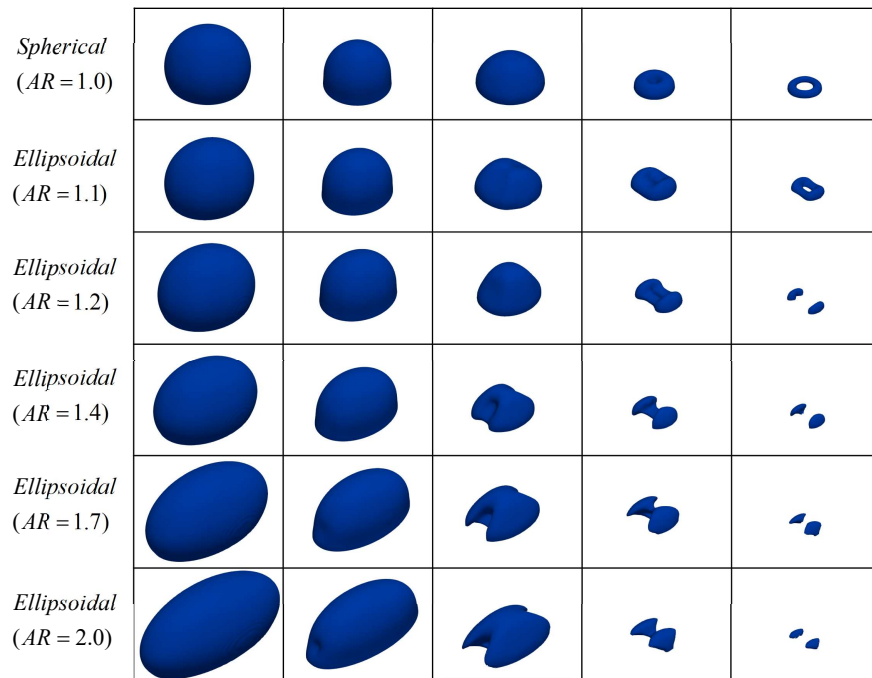


Figure 4.10: Collapse pattern of wall-mounted bubbles for all AR cases

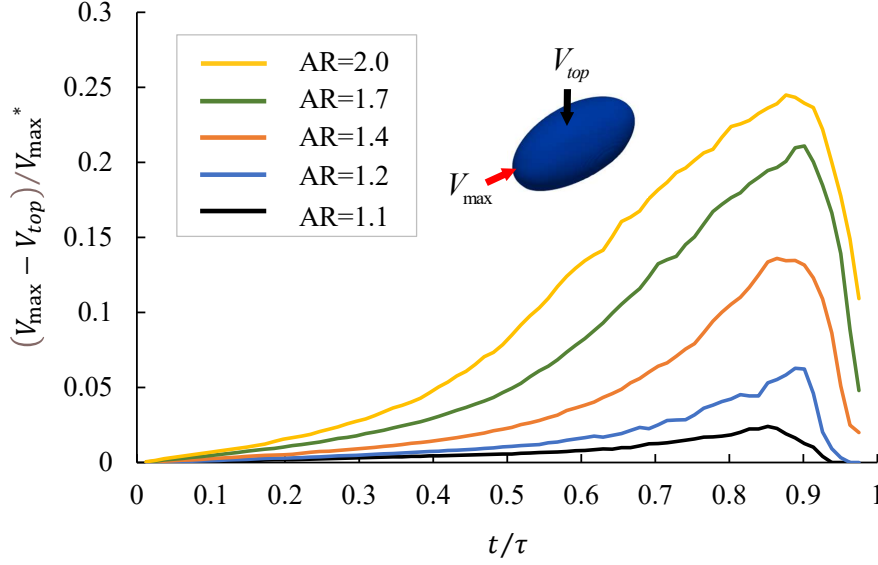


Figure 4.11: Magnitude difference between maximum jet and y-axis jet for all AR cases

difference of the two jets is extremely small just before collapse.

Here, the difference converges to zero at certain times for $AR=1.1$, 1.2 , and the smaller the AR , the faster the difference becomes zero. The convergence to zero implies that the y-axis jet becomes the maximum jet. To figure out this situation, we plot the position of the maximum jet (red arrow), the y-axis jet (black arrow) and the interface of the bubble in both yz cross-section in Fig. 4.12 and Fig. 4.13. In these cases, the position of the maximum jet moves from the point of initial maximum extension to the top of the bubble, and eventually the two jets coincide. Thereafter, the collapse pattern follows the spherical case. The bubble consequently has an asymmetric torus shape due to the change in the maximum jet position. These results show that when AR is close to 1, the relative magnitude of the initial dominant jet at the z -axis side of the bubble is not large enough to maintain the collapse pattern of ellipsoidal bubbles.

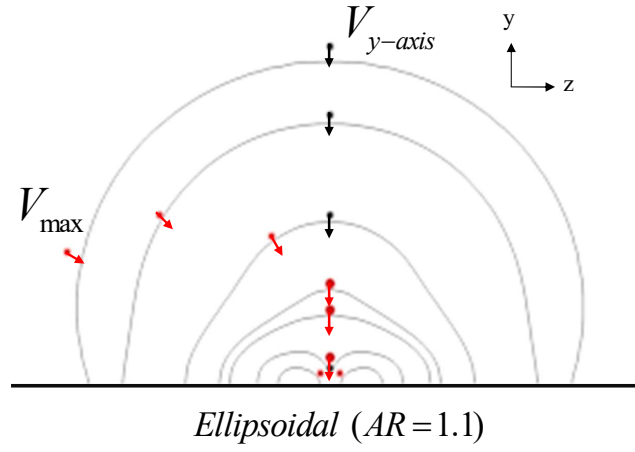


Figure 4.12: Interfaces of ellipsoidal bubble (black solid line) and position of the maximum jet (red arrow) and y-axis jet (black arrow) in yz cross-section (AR=1.1)

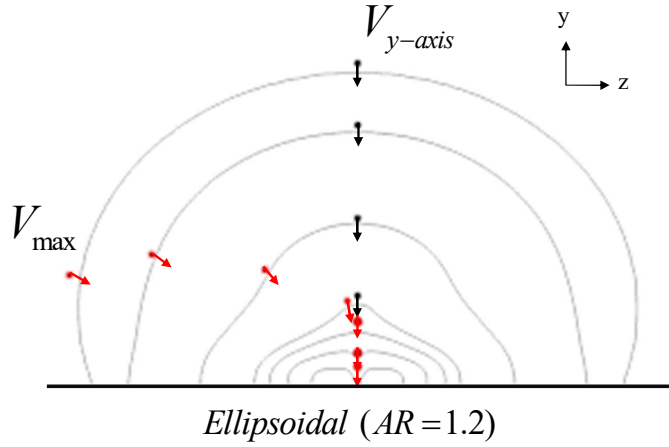


Figure 4.13: Interfaces of ellipsoidal bubble (black solid line) and position of the maximum jet (red arrow) and y-axis jet (black arrow) in yz cross-section (AR=1.2)

Chapter 5

Conclusion

In this study, a single cavitation bubble collapse in the free field is first simulated for validation and the significance of initial bubble shape has been investigated by comparing spherical and ellipsoidal cavitation bubbles in the situation where the bubble is attached to the wall. In the wall-attached bubble collapse, a delay effect by the wall basically occurs along with the radial direction jet. From this effect, the bubble forms a dome-shape in the early stage. In addition, the maximum jet, called the dominant jet, is developed at the initial maximum extension point, dominating the bubble collapse. For the spherical bubble, the dominant jet from the top of the bubble governs the collapse and the bubble collapses into a torus shape. From this collapse pattern, the impact on the wall spreads radially outward from the center of the wall. For the ellipsoidal bubble, different two jets governs the collapse. Among these, the relative magnitude of the dominant jet of them increases with the aspect ratio and the bubble collapses into two pieces, forming a lung-shape. From this collapse pattern, the jet impacts the wall in an asymmetric way, and the impact spreads from the center of the wall in the direction of the major axis of the bubble. On the other hand, if the aspect

ratio of the ellipsoidal bubble is close to 1.0, the position of the dominant jet moves from the side to the top of the bubble, and the bubble collapses into an asymmetric torus shape. This is because the relative magnitude of the dominant jet is too small to overcome the effect of the wall. From the results, it can be concluded that the collapse pattern of the bubble significantly depends on the position and the relative magnitude of the dominant jet determined by the aspect ratio.

Bibliography

- A. Aganin, M. Ilgamov, L. Kosolapova, and V. Malakhov. Dynamics of a cavitation bubble near a solid wall. *Thermophysics and Aeromechanics*, 23(2):211–220, 2016.
- J.-P. Franc and J.-M. Michel. *Fundamentals of cavitation*, volume 76. Springer science & Business media, 2006.
- E. Lauer, X. Hu, S. Hickel, and N. A. Adams. Numerical modelling and investigation of symmetric and asymmetric cavitation bubble dynamics. *Computers & Fluids*, 69: 1–19, 2012.
- W. Lauterborn and H. Bolle. Experimental investigations of cavitation-bubble collapse in the neighbourhood of a solid boundary. *Journal of Fluid Mechanics*, 72(2):391–399, 1975.
- S. Le Gac, E. Zwaan, A. van den Berg, and C.-D. Ohl. Sonoporation of suspension cells with a single cavitation bubble in a microfluidic confinement. *Lab on a Chip*, 7(12):1666–1672, 2007.
- K. Y. Lim, P. A. Quinto-Su, E. Klaseboer, B. C. Khoo, V. Venugopalan, and C.-D. Ohl. Nonspherical laser-induced cavitation bubbles. *Physical Review E*, 81(1):016308, 2010.

- V.-T. Nguyen and W.-G. Park. A free surface flow solver for complex three-dimensional water impact problems based on the vof method. *International Journal for Numerical Methods in Fluids*, 82(1):3–34, 2016.
- V.-T. Nguyen and W.-G. Park. A volume-of-fluid (vof) interface-sharpening method for two-phase incompressible flows. *Computers & Fluids*, 152:104–119, 2017.
- V.-T. Nguyen, T.-H. Phan, T.-N. Duy, D.-H. Kim, and W.-G. Park. Modeling of the bubble collapse with water jets and pressure loads using a geometrical volume of fluid based simulation method. *International Journal of Multiphase Flow*, 152:104103, 2022.
- A. Philipp and W. Lauterborn. Cavitation erosion by single laser-produced bubbles. *Journal of fluid mechanics*, 361:75–116, 1998.
- T. Požar, V. Agrež, et al. Laser-induced cavitation bubbles and shock waves in water near a concave surface. *Ultrasonics Sonochemistry*, 73:105456, 2021.
- M. Rodriguez, S. A. Beig, C. N. Barbier, and E. Johnsen. Dynamics of an inertially collapsing gas bubble between two parallel, rigid walls. *Journal of Fluid Mechanics*, 946:A43, 2022.
- H. J. Sagar and O. el Moctar. Dynamics of a cavitation bubble near a solid surface and the induced damage. *Journal of Fluids and Structures*, 92:102799, 2020.
- G. H. Schnerr and J. Sauer. Physical and numerical modeling of unsteady cavitation dynamics. In *Fourth international conference on multiphase flow*, volume 1. ICMF New Orleans New Orleans, LO, USA, 2001.
- T. Trummer, S. J. Schmidt, and N. A. Adams. Effect of stand-off distance and spatial

- resolution on the pressure impact of near-wall vapor bubble collapses. *International Journal of Multiphase Flow*, 141:103618, 2021.
- H. G. Weller, G. Tabor, H. Jasak, and C. Fureby. A tensorial approach to computational continuum mechanics using object-oriented techniques. *Computers in physics*, 12(6):620–631, 1998.
- D. L. Youngs. Time-dependent multi-material flow with large fluid distortion. *Numerical methods for fluid dynamics*, 1982.
- S. Zhang, A. Zhang, S. Wang, and J. Cui. Dynamic characteristics of large scale spark bubbles close to different boundaries. *Physics of Fluids*, 29(9):092107, 2017.

벽 부착 캐비테이션 기포의 붕괴에 관한 수치해석

본 논문에서는 기포가 벽에 부착된 상황에서의 구형 및 타원형 기포를 수치적으로 조사하였다. 시뮬레이션은 비압축성 2상 유동 솔버로 수행되었으며, 캐비테이션 기포 붕괴 과정의 급격한 변화에 있어서 기포 계면을 정확하게 추적하기 위하여 유체의 기하학적 부피 방법에 기반하여 캐비테이션 모델을 포함한 운송 방정식 모델을 사용하였다. 수치 모델은 Rayleigh 버블 붕괴 문제로 검증되며 결과는 해석해와 잘 일치하였다. 이어서, 벽에 부착된 캐비테이션 기포는 고정된 벽 거리 조건에 대해 시뮬레이션을 수행하였다. 구형 기포의 경우 수치 결과가 실험 결과와 잘 일치하며 기포가 원환면 형태를 띄며 붕괴되면서 벽에 대한 제트 충격이 벽의 중심에서 반지름 바깥 방향으로 확산되는 경향을 보였다. 반면 타원형 기포의 경우 종횡비에 관한 변수 연구가 수행되었다. 타원형 기포 붕괴에서는 두 개의 서로 다른 제트가 발생하며, 초기 기포의 종횡비는 이들 사이의 상대적 거동에 크게 영향을 주었다. 두 제트 중 상대적으로 높은 속도를 지니는 지배 제트가 붕괴 패턴을 주도하게 되며, 이에 따라 타원형 기포는 구형 기포와 달리 폐와 같은 모양을 형성하며 두 조각으로 분리되는 경향을 보였다. 이 때 벽에 대한 제트 충격은 벽의 중심으로부터 기포의 장축 방향으로 확산되었다. 반면 구형에 가까운 종횡비를 지니는 타원형 기포의 경우, 지배 제트의 크기가 상대적으로 작고 그 위치가 시간에 따라 변화하여 비대칭적인 원환면 형태를 띄며 붕괴되는 경향을 보였다. 이러한 결과로부터, 거품의 붕괴 패턴이 종횡비에 의해 결정되는 지배적인 제트의 위치와 상대적인 크기에 상당히 좌우되는 현상을 결론지었고 그 자세한 유동 특성을 수치적으로 제시하였다.

주요어: 수치해석, 다상 유동, 캐비테이션, 기포 붕괴

학번: 2021-29710